ACS APPLIED MATERIALS & INTERFACES

www.acsami.org

Research Article

Fluorine Labeling of Nanoparticles and In Vivo ^{19}F Magnetic Resonance Imaging

Juan Manuel Arango, Daniel Padro, Jorge Blanco, Sonia Lopez-Fernandez, Pilar Castellnou, Palmira Villa-Valverde, Jesús Ruiz-Cabello, Abraham Martin, and Mónica Carril*

Cite This: *ACS Appl. Mater. Interfaces* 2021, 13, 12941−12949

Read Online

ACCESS | Metrics & More | Article Recommendations | Supporting Information

ABSTRACT: Fluorinated nanoparticles have increasing applications, but they are still challenging to prepare, especially in the case of water-soluble fluorinated nanoparticles. Herein, a fluorine labeling strategy is presented that is based on the conjugation of custom-made small fluorinated building blocks, obtained by simple synthetic transformations, with carboxylated gold nanoparticles through a convenient phase-transfer process. The synthesis of four fluorinated building blocks with different chemical shifts in ^{19}F nuclear magnetic resonance and varied functionalities is reported, along with their conjugation onto nanoparticles. Fluorinated nanoparticles of small core size obtained by this conjugation methodology and by direct synthesis presented high transverse relaxation times (T_2) ranging from 518 to 1030 ms, and a large number of equivalent fluorine atoms per nanoparticle (340−1260 fluorine atoms), which made them potential candidates for ^{19}F magnetic resonance related applications. Finally, nontargeted fluorinated nanoparticles were probed by performing *in vivo* ^{19}F magnetic resonance spectroscopy (^{19}F MRS) in mice. Nanoparticles were detected at both 1 and 2 h after being injected. ^{19}F MRI images were also acquired after either intravenous or subcutaneous injection. Their fate was studied by analyzing the gold content in tissues by ICP-MS. Thus, the present work provides a general fluorination strategy for nanoparticles and shows the potential use of small fluorinated nanoparticles in magnetic-resonance-related applications.

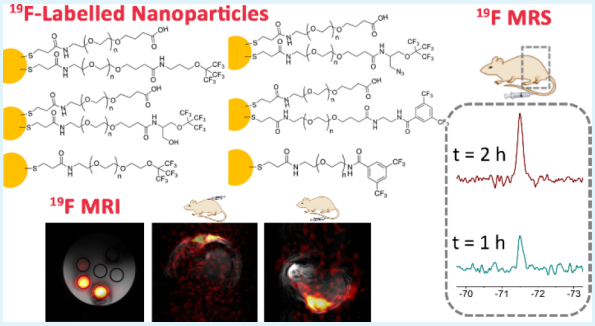

KEYWORDS: *fluorinated nanoparticles, fluorine labeling, ^{19}F MRS, ^{19}F MRI, in vivo*

1. INTRODUCTION

Fluorine is a unique atom that combines small atomic size with the highest electronegativity in the periodic table and forms one of the strongest bonds with carbon in organic chemistry.[1] It is also known to be highly hydrophobic and lipophobic, and fluorination is usually a challenging synthetic transformation.[2] Nonetheless, and despite its low occurrence in biological environments, fluorine is a very interesting atom from a (bio)medical perspective. For instance, in drug design, the inclusion of fluorine atoms in selected positions of organic molecules often substantially impacts the therapeutic performance of those molecules.[3] Enhancement of pharmacokinetic properties, metabolic stability, or increased cellular uptake are among the most commonly reported fluorine effects on drug candidates.[4] Likewise, fluorinated dendrimers were recently used for gene transfection because of such dendrimers' ability to accelerate endosomal escape and avoid degradation of the genetic material before reaching the cytosol, as compared to nonfluorinated tags.[5] Moreover, organic fluorine does not naturally occur in the human biological media for which it constitutes an exciting label or reporter. The absence of background signal allows for fluorinated species to be studied unequivocally and quantitatively by magnetic resonance spectroscopy related techniques, as long as sufficient local fluorine concentration is available. As a reporter, ^{19}F is a widely used label to study protein and sugar[6,7] or lipid[8] interactions by ^{19}F nuclear magnetic resonance (^{19}F NMR). In addition, ^{19}F magnetic resonance imaging (^{19}F MRI), based on imaging exogenous fluorinated probes *in vivo*, is a versatile diagnosis technique complementary to conventional ^{1}H MRI.[9] The lack of fluorine background allows for the design of ratiometric[10] and quantitative smart contrast agents[11] that are difficult to achieve for ^{1}H MRI.[12] However, the applicability of ^{19}F MRI is currently limited by the detection sensitivity of the MRI technique and the need for a high local concentration of fluorine, for which the design of highly fluorinated probes is an active field of research.[13−17]

Received: January 20, 2021
Accepted: February 22, 2021
Published: March 11, 2021

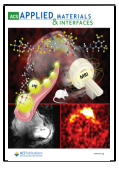

https://dx.doi.org/10.1021/acsami.1c01291
ACS Appl. Mater. Interfaces 2021, 13, 12941−12949

Despite its interesting features, the prospects of fluorine in nanoparticle (NP) design for nanomedicine are somehow limited for several reasons, namely, (i) the high hydrophobicity of fluorinated molecules, (ii) the sometimes challenging synthesis of those, (iii) the need for high local concentration of fluorine for magnetic resonance (MR) applications, and (iv) the usually low relaxation times due to NP intrinsic structural design. Thus, examples of fluorinated NPs composed of a metal core and fluorinated ligands that are water soluble are scarce in the literature.[18−20] In this context and in the last years, we and others have overcome the fluorine hydrophobicity challenge and prepared fluorinated inorganic nanoparticles that are totally or partially dispersible in water by different strategies. Such fluorinated NPs have been utilized in other nanomedicine related fields, such as to study protein corona in complex environments,[21,22] as potential contrast agents in ^{19}F MRI,[18,23,24] or as vehicles for enzyme transport, and delivery through fluorine-based interactions[25−27] (Figure 1C D). The strategies we used so far to introduce fluorinated

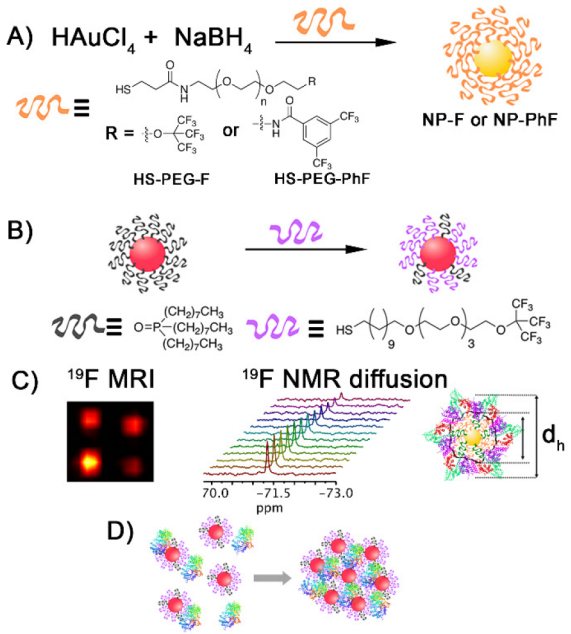

Figure 1. (A) Synthesis of fluorinated NPs by direct synthesis method. (B) Synthesis of fluorinated quantum dots by ligand exchange method. Summary of applications of fluorinated NPs in (C) magnetic resonance field, such as contrast agents in ^{19}F MRI and as protein corona reporters in ^{19}F NMR-based diffusion. (D) Illustration of the use of fluorinate quantum dots as enzyme encapsulation and delivery platforms.

moieties on the surface of inorganic NPs were either via the direct synthesis of gold NPs from chloroauric acid in the presence of custom-designed fluorinated-thiolated ligands and sodium borohydride (Figure 1A),[21−23] or by ligand exchange on presynthesized quantum dots with fluorinated-thiolated ligands to prepare fluorinated quantum dots (Figure 1B).[25−28] These methods, although useful, are limited to thiol-binding nanomaterials, and for the case of ligand exchange, a significant excess of ligand is needed and full exchange is hardly ever achieved.

To avoid these issues, researchers have based many fluorinated formulations in the field of nanomedicine on the encapsulation of highly hydrophobic perfluorocarbons in emulsions of about 200 nm or larger.[29] Nonetheless and except for its role as a label for magnetic resonance (MR), to benefit from the presence of fluorine, it needs to be exposed (not encapsulated) to be able to interact with biointerfaces and receptors,[30] as has been recently demonstrated for fluorinated polymer NPs.[31] Hence, the development of fluorination strategies for macro(bio)molecules and colloids for biomedical applications that expose fluorine on their surface is an interesting research field. The pursuit of more general synthetic methods for fluorination of NPs would be useful to develop new fluorinated NPs with potential applications in multiple areas, as mentioned before. We present herein a simplified synthetic tool for the preparation of fluorinated NPs based on the conjugation of fluorinated building blocks of simple preparation onto the surface of carboxylated NPs. Such conjugation took place through a facile phase transfer protocol, which rendered water-soluble fluorinated NPs with interesting MR features. We showed that small core NPs obtained by either conjugation or direct synthesis method convey a high local content of fluorine per NP while allowing for the coexistence of other functionalities on the NP's surface. In addition, we proved that fluorinated small gold NPs are suitable candidates for *in vivo* ^{19}F magnetic resonance spectroscopy (^{19}F MRS) and imaging (^{19}F MRI) in mice.

2. RESULTS

2.1. Fluorine Conjugation onto NPs. The conjugation of small and simple fluorinated amino-ending building blocks (**F**, **F/OH**, **F/N$_3$**, and **PhF**) on a model carboxylated gold NP (**NP-COOH**) to prepare novel fluorinated NPs (**NP+F**, **NP+F/OH**, **NP+F/N$_3$**, and **NP+PhF**) was optimized (Figure 2). A simple phase transfer method was used to bind fluorinated building blocks onto **NP-COOH**, which also greatly simplified the purification of the so-obtained NPs.

On the one hand, small gold NPs of about 3 nm in core diameter functionalized with carboxyl moieties were chosen as

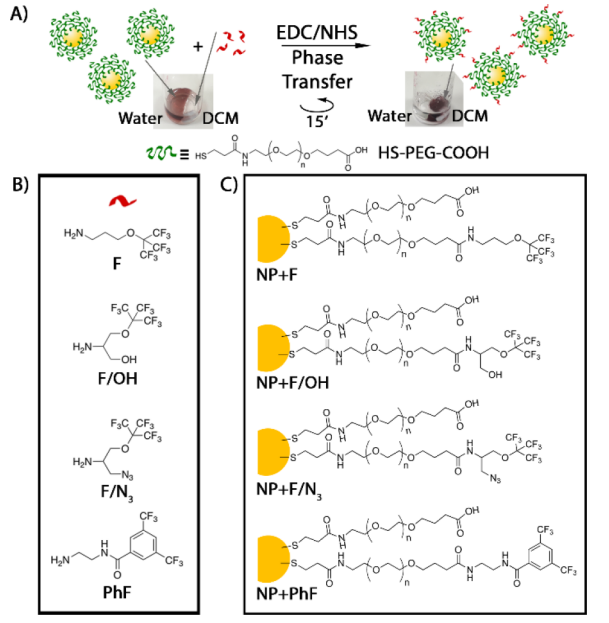

Figure 2. (A) Scheme of the conjugation method onto **NP-COOH** through a phase transfer process reported herein. (B) Structures of fluorinated building blocks **F**, **F/OH**, **F/N$_3$**, and **PhF**. (C) Illustration of obtained **NP+F**, **NP+F/OH**, **NP+F/N$_3$**, and **NP+PhF**.

https://dx.doi.org/10.1021/acsami.1c01291
ACS Appl. Mater. Interfaces 2021, 13, 12941−12949

the model NP because of their simple synthesis and the plethora of techniques available for their characterization, especially for the use of NMR,[32] which is useful for determining the amount of fluorine incorporated through ^{19}F NMR. Commercially available thiol and carboxyl ending PEG ligand (**HS-PEG-COOH**) was mixed with chloroauric acid in the presence of sodium borohydride to afford **NP-COOH** with a gold core radius r_c of 1.54 ± 0.54 nm, after transmission electron microscopy (TEM) analysis. These NPs were stored in water until further use, and the concentration of the NP solution was obtained from the gold content analysis by inductively coupled plasma mass spectrometry (ICP-MS). Additionally, by combining TEM with ICP-MS data, it was possible to estimate that the number of ligands per **NP-COOH** was 140, which corresponded to approximately 5 ligands per nm^2 of the NP's surface. The good colloidal stability of the so-obtained NPs was also assessed by ultraviolet−visible spectroscopy (UV−vis), which displayed a plasmon resonance band at λ = 510 nm, as expected for that core size.

On the other hand, we synthesized fluorinated building blocks with different chemical shifts in ^{19}F NMR (**NP+F** and **NP+PhF**) or that carry different functional groups (**NP+F/OH** and **NP+F/N_3**), prone to be derivatized if desired. Amino-ending fluorinated small building blocks **F**, **F/OH**, and **F/N_3** were prepared by simple synthetic transformations from phthalimide protected amino starting groups, and the perfluorinated tert-butoxide moiety was introduced via a Mitsunobu reaction to afford the final amino unprotected products in two or three reaction steps. Building block **PhF**, with a different fluorinated moiety, was obtained through the reaction of a diamino derivative and a conveniently functionalized acyl chloride. Except for the latter, the rest of the fluorinated building blocks were volatile, and hence they were stored in dichloromethane solution after reaction and workup. The amount of each building block in solution was calculated by ^{19}F NMR calibration of the fluorine signal intensity with respect to a fixed and known amount of trifluoroacetic acid (Figures S1 and S2). All the synthetic and characterization details are described in the Supporting Information.

These fluorinated building blocks presented an amino group that could be readily reacted with carboxyl groups on the NP surface through EDC/NHS activation. Such a methodology is straightforward, compatible with both water and organic solvents, and widely applied to the functionalization of NPs with biomolecules because of the usually mild reaction conditions.[33,34] In our protocol, carboxylated NPs in water were initially mixed with EDC/NHS and allowed to react for 30 min to activate the carboxyl groups on the NP surface. Subsequently, the selected fluorinated building block in dichloromethane (DCM) was added, and the mixture was stirred vigorously to promote maximum contact between the two immiscible phases, the red aqueous one containing the **NP-COOH** and the transparent organic one with the selected fluorinated compound. In our particular setting, because of the fluorination of the NPs, a phase transfer takes place from the aqueous to the organic phase, which is easily observed due to the red color transfer from the top aqueous phase to the bottom organic one. Such a process happened within the first 15 min after amine addition, but the reaction was allowed to stir overnight to achieve the maximum conjugation yield.

The reaction conditions were optimized for each building block to obtain the highest conjugation yield, defined as the percentage of ligands functionalized with fluorinated building blocks per each NP. However, with this system, a maximum conjugation yield for each building block was achieved no matter how much amine was added (27−51%, Table 1), most likely due to steric hindrance of the already conjugated fluorinated building blocks that may hamper the inclusion of new ones. The increase in the EDC/NHS amount did not improve the yield, and in some cases, it even led to partial aggregation of the gold nanoparticles, as observed by UV−vis (Table 1, entry 1). Frequently, this type of conjugation takes place under more or less mild basic conditions. However, the use of a buffered solution at pH 9 did not have a clear positive impact on the yield of the reaction (Table 1, entry 4 vs 5).

Table 1. Selection of Conjugation Conditions Tested[a]

entry	F^c	resulting NP	yield (%)[d]
1[b]	0.1	**NP+F**	[e]
2	0.3	**NP+F**	[e]
3	0.4	**NP+F**	38
4	0.9	**NP+F**	36
5	0.9	**NP+F**	39[f]
6	0.4	**NP+F/OH**	15
7	0.6	**NP+F/OH**	27
8	0.4	**NP+F/N_3**	35
9	0.6	**NP+F/N_3**	51
10	0.4	**NP+PhF**	14[f]
11	0.8	**NP+PhF**	47

[a]286 equiv. of EDC with respect to COOH moles and 3 NHS equivalents with respect to EDC were used in each reaction. [b]857 equiv. of EDC were used. [c]*F* refers to fluorinated building block equivalents with respect to EDC. [d]Percentage of ligands modified with fluorinated building blocks in each NP. [e]Aggregation detected by UV−vis. [f]Borate buffer saline (BBS buffer) at pH 9 was used in the aqueous phase.

2.2. Characterization of Fluorinated NPs Obtained by the Conjugation Method. After the synthesis, **NP+F**, **NP+F/OH**, **NP+F/N_3**, and **NP+PhF** were purified by phase separation, and the now transparent aqueous layer was discarded. The fluorinated NPs were in the organic phase after the reaction, so dichloromethane was removed by evaporation. The dried, fluorinated NPs were easily redispersed in water and extensively washed through filtration to remove all reagents and unbound fluorinated building blocks (Figure S3). The dual solubility of the so-obtained NPs, which could be both dispersed in dichloromethane and water, was enabled by the 3 kDa PEG linker present in the ligand structure. The absence of unbound fluorinated building blocks was confirmed by ^{19}F NMR, taking advantage of the different chemical shifts of the fluorine atoms in the free building blocks (δ = −71.87 ppm (**F**); −71.71 ppm (**F/OH**); −71.89 ppm (**F/N_3**); −62.73 ppm (**PhF**)) and in the corresponding fluorinated NPs (δ = −71.41 ppm (**NP+F**); −71.38 ppm (**NP+F/OH** and **NP+F/N_3**); −63.61 ppm (**NP+PhF**)) (Figure 3A). Subsequently, thorough characterization by different techniques was performed. UV−vis spectra showed minimal variations between the parent **NP-COOH** and the newly obtained fluorinated NPs, and all surface resonance plasmon (SPR) wavelengths ranged from 509 to 511 nm (Figure 3B). This feature means that the optimized conjugation conditions did not affect the core of the NPs. This was further confirmed by TEM analysis that showed that the cores' sizes remained unchanged after the conjugation (Figure 3C, D). Diffusion

https://dx.doi.org/10.1021/acsami.1c01291
ACS Appl. Mater. Interfaces 2021, 13, 12941−12949

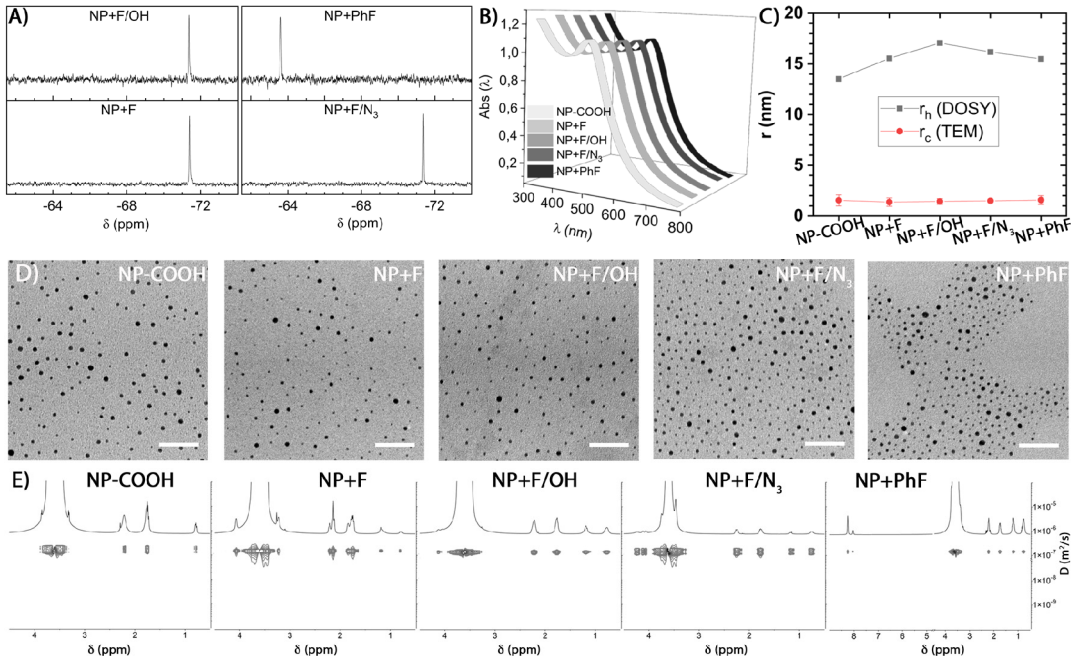

Figure 3. (A) ^{19}F NMR spectra of **NP+F**, **NP+F/OH**, **NP+F/N$_3$**, and **NP+PhF**. (B) UV−vis spectra of **NP-COOH**, **NP+F**, **NP+F/OH**, **NP+F/N$_3$**, and **NP+PhF**. (C) Graph showing the core radius (r_c) and the hydrodynamic radius (r_h) of each NP as obtained from TEM or DOSY analysis, respectively. (D) TEM micrographs of all NPs showing the gold cores, scale bar corresponds to 50 nm. (E) DOSY spectra for all NPs, showing that all signals in the spectra belong to the NPs and the diffusion coefficient for each NP.

ordered spectroscopy (DOSY) measurements were performed to calculate the diffusion coefficient of NPs in water before and after conjugation. From the diffusion coefficient and through the Einstein−Stokes relation, it was possible to calculate the hydrodynamic size of each NP (Figure 3C, E).[21,22,32] It was observed that the conjugation of **F** and **PhF** produced a size increase of 2 nm in the hydrodynamic radius (r_h) as compared to the size of **NP-COOH** (r_h = 13.53 nm), and the conjugation of branched more bulky **F/OH** and **F/N$_3$** afforded an extra size increase of 3.54 and 2.65 nm, respectively (Figure 3C and Table S3). The data obtained from DOSY agreed with those obtained from dynamic light scattering (DLS) (Figure S7).

We studied the storage stability of the so-obtained fluorinated NPs over time from two points of view, that is leaching of fluorine and changes in hydrodynamic size. For this reason, ^{19}F NMR spectra of one-year-old samples were performed, and neither changes in the fluorine conjugation ratio nor the appearance of new signals were detected because of the degradation of fluorinated moieties. Also, DLS measurements were performed on the same samples, and it was observed that NPs remained mostly unchanged in terms of hydrodynamic size. It must be noted that samples were not submitted to any particular stability test and instead were simply stored between 4 °C and room temperature for about one year (Table S3). Also, XPS measurements showed the presence of Au (0), Au−S bonds, and fluorine. However, penetration depth limitations of the technique and the thick organic coating on the NPs did not allow us to rule out the presence of small amounts of oxidized gold or sulfur species (see Figure S8).

2.3. Magnetic Resonance Properties of Fluorinated NPs. We also studied whether the conjugated fluorinated building blocks could afford fluorinated NPs with interesting properties as labels for magnetic resonance derived applications. For this purpose, longitudinal (T_1) and transverse (T_2) relaxation times of **NP+F**, **NP+F/OH**, **NP+F/N$_3$**, and **NP+PhF** were measured. Ideally, long T_2 values are desirable to avoid signal intensity loss, whereas short T_1 values are important to reduce acquisition times and increase the number of scans per unit time. In our examples, we obtained T_1 values ranging from 812 to 997 ms and T_2 values between 518 and 766 ms (Figure 4 and Table S5). For the longitudinal relaxation times, our NPs are within the average values reported for other fluorinated probes. Interestingly, the transverse relaxation times are well above the average (Figure

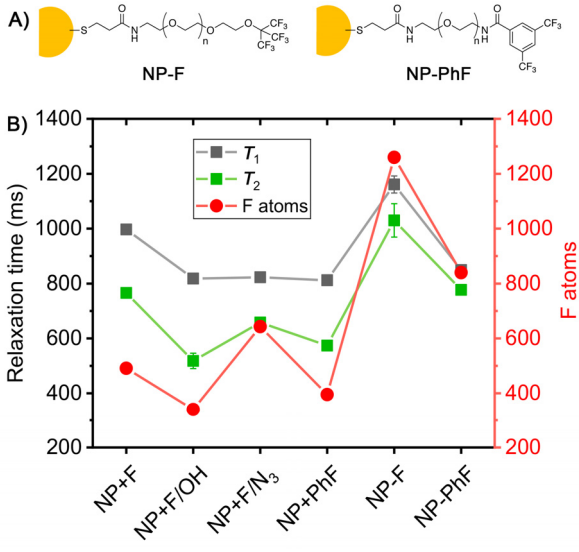

Figure 4. (A) Illustration of **NP-F** and **NP-PhF**, obtained by direct method synthesis. (B) Plot of the T_1, T_2, and fluorine atoms (F atoms) per NP for each NP. For relaxation times, the mean and standard deviation of two independent measurements are shown.

https://dx.doi.org/10.1021/acsami.1c01291
ACS Appl. Mater. Interfaces 2021, 13, 12941−12949

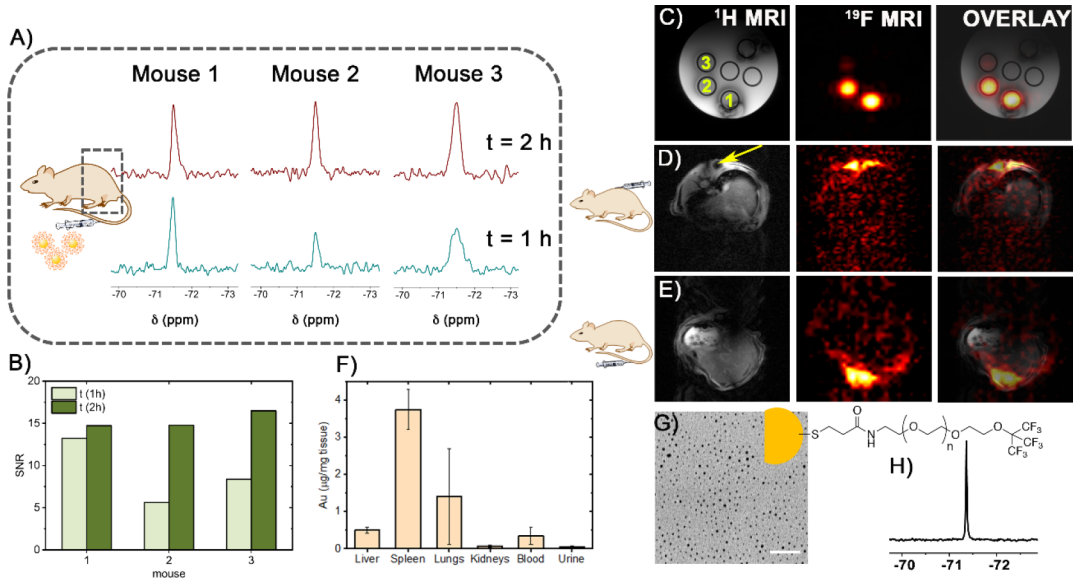

Figure 5. (A) ^{19}F MRS spectra of three mice injected with **NP-F** 1−2 h after injection. An exponential line broadening of 15 Hz was applied to all spectra when analyzed in *Mnova*. (B) SNR of each spectrum as obtained with the *Mnova* software SNR tool. (C) MRI phantom image of **NP-F** at three different concentrations of fluorine: (1) 21, (2) 15, and (3) 1.5 mM. The rest of the tubes contained water. (D) MRI images after subcutaneous localized back injection of **NP-F** (21 mM in fluorine). The yellow arrow on the ^{1}H MRI image shows the injection site. The mouse's back was placed on the surface coil. (E) MRI image of the liver after tail vein injection of **NP-F** (21 mM in fluorine). The mouse's belly was placed on the surface coil. (F) ICP-MS analysis of the gold content of extracted tissues and fluids from three mice (liver, spleen, lungs, kidneys, blood, and urine) represented in terms of gold content per unit weight of tissue or fluid. (G) TEM micrograph of **NP-F**. (H) ^{19}F NMR spectra of **NP-F**.

S12). Considering the highest conjugation yield achieved for each of them and knowing from ICP-MS data that each NP had 140 ligands, we could estimate the number of fluorine atoms per NP, which ranged from 340 to 643 and represents the localized amount of equivalent fluorine atoms that a single NP conveys by itself, as long as it remains intact.

For comparison purposes, similar fluorinated NPs already reported by us (**NP-F** and **NP-PhF**) were prepared by the direct synthesis method (Figure 1A) and shown in Figure 4A.[21−23] The so-obtained NPs were very similar in core size (r_c = 1.47 ± 0.43 nm (**NP-F**) and 1.60 ± 0.45 nm (**NP-PhF**)) to those obtained by the conjugation method and slightly smaller in hydrodynamic size because of the shorter length of the employed ligands (r_h = 8.99 ± 0.07 nm (**NP-F**) and 9.82 ± 0.10 nm (**NP-PhF**)). The ligand density for both NPs was also around 5 ligands per nm^2 of gold core surface, as obtained by ICP-MS analysis. Using the direct synthesis method with already synthesized fluorinated PEGylated ligands (Scheme S5), all ligands on the surface of the NPs were fluorinated. Hence, by this method, we could achieve fluorine loadings of up to 840 and 1260 atoms per **NP-PhF** and **NP-F**, respectively. The relaxation times obtained for these NPs were higher for **NP-F** (T_1 = 1161 ms and T_2 = 1030 ms) and quite similar for **NP-PhF** but higher in general (T_1 = 849 ms and T_2 = 777 ms) when compared with those obtained for NPs prepared by conjugation method (Figure 4B and Table S5).

2.4. *In Vivo* ^{19}F MRS and ^{19}F MRI Experiments. To test the potential *in vivo* applicability of small fluorinated NPs of the type described herein in terms of ^{19}F signal detection, we injected three mice with a selected fluorinated NP and *in vivo* nonlocalized ^{19}F MRS (magnetic resonance spectroscopy) was performed. As we did not have any previous reference work for the *in vivo* use of such NPs and being SNR (signal-to-noise ratio) one of the significant limitations of ^{19}F-based MR detection, we chose the most favorable scenario, that is, the use of a fully fluorinated gold NP that maximized the fluorine atoms per NP (**NP-F** with 1260 F atoms/NP) and a high concentration of those NPs (18 μM in NPs, approximately 23 mM in fluorine). **NP-F** was prepared as described previously by us,[21−23] with a gold core radius r_c of 1.47 ± 0.43 nm as obtained by TEM (Figure 5G), and a hydrodynamic radius r_h of 8.99 ± 0.07 nm as measured by DOSY. The UV−vis spectrum showed the typical surface plasmon band at 511 nm, which is expected for this size of NP, and displayed colloidal stability. The concentration of **NP-F** solution was measured by ICP-MS to obtain the gold content. The fluorine concentration was obtained by assuming that each **NP-F** had around 140 ligands (approximately 5 ligands/nm^2 of the NP's surface), as calculated herein (see the Supporting Information) and previously,[21−23] and by combining these data with the NP concentration obtained by ICP-MS. As expected, **NP-F** displayed a single narrow peak in ^{19}F NMR with a chemical shift δ of −71.36 ppm (Figure 5H) and had T_1 and T_2 values around 1 s, as shown previously (Figure 4B).

The aim of this experiment was to test the possibility of a ^{19}F signal detection in vivo by using our fluorinated NPs, so no targeting was introduced in **NP-F** and no particular tissue was selected for spectroscopy. Instead, we performed ^{19}F MRS of the bottom half of the mice at 1 and 2 h after intravenous injection in the tail. That area was selected on the basis of the assumption that NPs would mostly be eliminated through either hepatobiliary or renal excretion pathways. In all three mice, we observed a clear peak corresponding to our NPs at 1 and 2 h after injection, as NPs accumulated in tissues (Figure 5A). Each spectrum was obtained in about 16 min, although the signal could be already detected after a few scans, and the mice were not moved between the first and second scan. The SNR increased between the first and second scan, as one could expect because of the increased accumulation of NPs in tissues, and it was particularly noticeable in two of the three mice

https://dx.doi.org/10.1021/acsami.1c01291
ACS Appl. Mater. Interfaces 2021, 13, 12941−12949

(Figure 5B). It must be noted that the NPs employed in this study and those reported in this paper have chemical shifts that do not interfere with signals around −80 ppm coming from isoflurane and metabolites derived from it, which is a commonly used fluorinated anesthetic drug. After the last scan, mice were sacrificed, and several tissues and fluids were collected, namely liver, spleen, lungs, kidneys, blood, and urine. After lyophilization, the extracted tissues and fluids, together with the gold NPs in them, were digested first with nitric acid and later with aqua regia, and the gold content was analyzed by ICP-MS. The highest amount of gold in absolute numbers was detected in the spleen and liver (Figure S13). However, the organ's amount of gold per weight was substantially larger for the spleen than for the liver (Figure 5F). Interestingly, there were still gold NPs detected in extracted blood, showing that the circulating times exceeded 2 h for these NPs (Figure 5F and Figure S13).

Subsequently, we tested the performance of **NP-F** as ^{19}F MRI contrast agents. Phantoms of **NP-F** solutions at different concentrations (21, 15, and 1.5 mM in fluorine) were prepared. A 7 T MRI scanner with a surface quadrature coil was used for data acquisition, and hence sensitivity was greater for the samples closer to the coil. More concentrated solutions (21 and 15 mM) were already detectable after 1 min scan (Figure S14), but after 2 h, even the 1.5 mM solution was slightly noticeable (Figure 5C). Initially, for the in vivo experiments, an **NP-F** localized subcutaneous injection on the mouse's back was performed, followed by imaging acquisition. NPs were already detected after a very short scanning time (4 min) using this surface coil placed on the injection site and a FLASH sequence (Figure 5D). Longer acquisition times provided better SNR, as shown in Figure S15. Subsequently, intravenous injection in the tail vein led to a nontargeted biodistribution of **NP-F**. As expected, 1 h after injection partial accumulation in the liver was already detectable using the same surface coil placed on the mouse's belly and a FLASH sequence after 14 min of acquisition (Figure 5E).

3. DISCUSSION

Many NP synthetic methods are based on precoating strategies, after which NPs are functionalized by ligand exchange or polymer coating.[35] To avoid the waste of costly and sometimes synthetic challenging fluorinated ligands, we developed a method based on the use of small, easy-to-prepare fluorinated building blocks, based on commercially available perfluorinated *tert*-butanol to avoid complex fluorination steps and their conjugation onto preformed carboxylated NPs. By customized design of the fluorinated building blocks (**F**, **F/OH**, **F/N$_3$**, and **PhF**), our methodology allowed the preparation of fluorinated NPs with substantially different chemical shifts in ^{19}F NMR (**NP+F** and **NP+PhF**) or the simultaneous introduction of other functional groups (**NP+F/OH** and **NP+F/N$_3$**). This methodology enabled the conjugation of at least 340 fluorine atoms per NP and up to 643 fluorine atoms (Table S5). The employed reaction conditions and phase transfer process were mild and did not affect the colloidal stability of the resulting fluorinated NPs. A number of NMR based techniques were used to characterize them, such as the fluorine content through ^{19}F NMR signal integration or the hydrodynamic size by DOSY. It must be noted that the so-obtained fluorinated NPs had exceptionally high T_2 values (above 500 ms), above the average of reported fluorinated probes, which makes them potentially interesting as fluorinated probes for ^{19}F MRI. On the contrary, obtained T_1 values were within the average of reported systems, although ideally shorter times would be of greater interest (Figure S12).

The direct synthesis method previously reported by us produced fluorinated NPs (**NP-F** and **NP-PhF**)[21,22] of similar size, colloidal stability, and MR properties as those reported herein, but with higher fluorine content per NP, as all the ligands on the surface were fluorinated. Regarding the relaxation times, **NP-F** obtained by direct synthesis afforded higher values for both T_1 and T_2, and **NP-PhF** had relaxation time values more similar to those obtained for NPs prepared by conjugation method, although still higher in general (Figure S9B). Nonetheless, although the obtained T_1 values are within the average of reported values, the high T_2 values of the fluorinated NPs presented herein are usually hard to achieve for fluorinated probes and are most likely a consequence of 2 factors: (i) the presence of PEG ligands that conferred water solubility and high flexibility to the fluorine moieties, and (ii) the small size of the gold core that provides sufficient curvature to its surface to enable fluorine mobility. It must be noted that although in the direct synthesis method all the ligands on the NP surface had the same length, in the NPs obtained by the conjugation method, **NP+F**, **NP+F/OH**, **NP+F/N$_3$**, and **NP+PhF**, the fluorinated building blocks protrude from the NP because they form longer ligands than only **HS-PEG-COOH**. This effect might provide some space for the fluorine atoms to avoid the surrounding water and perhaps hide in more or less hydrophobic pockets that could be formed in the outer shell of the NPs. This could afford a plausible explanation for the lower relaxation times of NPs prepared by conjugation of fluorinated building blocks with respect to their sister NPs obtained by direct synthesis, despite being all of them very similar in terms of physical features and structure.

The applicability of fluorinated small gold NPs in MR related techniques, beyond the characterization of essential parameters such as the relaxation times, was evaluated. In this sense, **NP-F** was successfully detected *in vivo* in three mice by ^{19}F MRS. As a proof of concept and given the lack of targeting of **NP-F**, very high fluorine concentrations were used. Also, ^{19}F MRI images were obtained within very reasonable scanning times both after localized subcutaneous injection and after systemic injection, as they started to accumulate in the liver. Because the signal was already clearly detected both by ^{19}F MRS and ^{19}F MRI after a few scans, we envisage that lower systemic doses will be required for targeted, localized spectroscopy/imaging in a pathological animal model. However, that is yet to be tested. The biodistribution profile was the expected for nontargeted NPs in healthy mice. We believe that spleen and liver accumulation might be reduced in the future by reducing the injected dose, which was substantially high, and by slightly decreasing the hydrodynamic size of **NP-F**. The detection of gold by ICP-MS in blood after more than 2 h suggests that **NP-F** could have reasonable circulating times, as has been generally observed for PEGylated NPs, which is a promising feature for their applicability *in vivo*, although it needs to be further explored.

4. CONCLUSION

The fluorine conjugation strategy reported herein poses an alternative for the fluorination of other nanomaterials in which efficient direct synthesis with fluorinated ligands is not possible because of either challenging fluorinated ligand design or NP synthetic method limitations. Thus, given the plethora of

https://dx.doi.org/10.1021/acsami.1c01291
ACS Appl. Mater. Interfaces 2021, 13, 12941−12949

carboxylated NPs in the literature, the presented methodology could be considered as a general method for fluorination of NPs, particularly when exposure of the fluorine on the surface is required. However, because of the different ligand composition and structures of other reported carboxylated NPs, we envisage that the conjugation process and purification may have to be optimized and adapted for each particular case. By simplifying the fluorination strategy and adapting it to the modification of such a common functional group as the carboxyl moiety, the possibility to extend this methodology to label any kind of NP (not only gold-based), nanosystems or macromolecules is now open, as long as they have carboxyl groups available. Thus, nanomaterials with new surface designs and applications could be produced, beyond the nanomedicine field. Moreover, we proved that NPs of the types reported herein can be used for *in vivo* ^{19}F MRS and ^{19}F MRI. Although preliminary, these results set the pavement for future applications of fluorinated NPs *in vivo*, but more detailed studies are yet to be conducted before their use as diagnosis tools in ^{19}F MR related techniques. For this particular field of application, the use of small core-sized NPs along with PEGylated ligands was key to achieving high probe concentrations and good relaxation times for fluorine.

5. EXPERIMENTAL SECTION

All experimental procedures are fully described in detail in the Supporting Information. Here we include a few representative procedures.

Fluorine Conjugation Method for the Preparation of NP+F. Typical Procedure. **NP-COOH** in MilliQ water (690 μL, 0.33 μM) was placed in a screw capped vial with a magnet. A solution of NHS in water (3.21 mg in 25 μL) was added onto **NP-COOH** followed by a solution of EDC·HCl in water (1.78 mg in 25 μL). The mixture was allowed to stir capped at r.t. for 30 min to activate carboxyl groups. CH_2Cl_2 (263 μL) was then added to the activated NPs followed by building block **F** dissolved in CH_2Cl_2 (82 μL, 47.7 mM), and the reaction was tightly capped to avoid solvent evaporation. The reaction was allowed to stir at the maximum possible speed at r.t. After 15 min, the phase transfer of the NPs from the aqueous phase to the organic already took place; however, the reaction was left stirring overnight to achieve the maximum conjugation possible. The next morning, the reaction mixture was transferred to an Eppendorf and centrifuged for a short time to improve phase separation. Following this procedure, the organic phase was washed twice with water and then transferred to a glass vial and left open to evaporate. In this step, most of unreacted building block **F** also evaporated. A flush of compressed air was used to finally ensure that all CH_2Cl_2 was gone and then the resulting NPs were resuspended in MilliQ water. This solution was transferred to 100 kDa MWCO amicon filters and washed thoroughly (at least seven times) with MilliQ water to render NP+F.

Direct Synthesis Method for the Preparation of NP-F. Typical Procedure. **HS-PEG-F** ligand (1125 μL of a 2.5 mM solution in CH_2Cl_2) was added to 50 mL of CH_2Cl_2 while stirring at r.t. Subsequently, a 0.1 M solution of $NaBH_4$ was freshly prepared with ice-cold methanol and allowed to stand for 1 min. During that minute, a freshly prepared solution of $HAuCl_4$ (250 μL, 25 mM) in ice-cold methanol was added to the reaction mixture. One minute after the preparation of $NaBH_4$ solution, the latter (313 μL, 0.1 M) was added dropwise to the ligand/gold mixture. The reaction was stirred for 30 s and then allowed to stand overnight without stirring at r.t. Hereby the solution was capped to avoid solvent evaporation. The next day, the solvent was evaporated in a rotary evaporator, and the NPs were resuspended in water and then purified by centrifugation. First, NPs were centrifuged twice at 1.5×10^5 g for 2 h to remove unbound ligand and very small NPs, which remained in the supernatant and were discarded. Second, the so-obtained pellet was resuspended in water and centrifuged twice at 5×10^4 g for 30 min to remove aggregates and bigger NPs that precipitated at that speed and were discarded. Hence, NPs that remained in the supernatant were kept for further experiments. Prior to their use in vivo, **NP-F** was concentrated down to 17 μM (NP concentration) in water using centrifugal filters (100 kDa MWCO).

Transverse and Longitudinal Relaxation Times (T_2 and T_1) Measurement of Fluorine. ^{19}F T_2 measurements were performed using Bruker's standard CPMG sequence at 470.55 MHz with the following parameters: TR = 12.0 s, 16 echo times covering a range between 0.02 and 24 s, SW = 17 ppm, NS = 24, DS = 4 and 32K points. T_1 measurements were performed using an inversion recovery method with Bruker's t1ir sequence at 470.55 MHz with the following parameters: TR = 12.0 s, 16 inversion times (5, 4.5, 4, 3.5, 3, 2.5, 2, 1.5, 1, 0.800, 0.500, 0.300, 0.200, 0.100, 0.050, 0.001 in seconds), SW = 20 ppm, NS = 64, DS = 4 and 32K points, in a mixture of water and D_2O.

^{19}F MRS Acquisition Protocol. ^{19}F MRS experiments were performed in a Bruker BioSpec 11.7 T magnetic resonance scanner with 16 cm bore for small rodents (Bruker Biospin) along a 9 cm shielded gradient insert capable of 750 mT/m. The acquisition of ^{19}F MRS spectra was done employing a 40 mm inner diameter ^{1}H/^{19}F coil, which also allowed the acquisition of a reference proton image before the ^{19}F MRS spectra recording. All ^{19}F nonlocalized spectra were acquired without proton decoupling and applying the following parameters: TD 4K, SW 10 ppm, 8 dummy scans, 660 averages, TR 1.8 s, and with a total acquisition time of 16 min. All spectra were processed with zero filling, and applying an exponential line broadening of 15 Hz. Every animal was scanned twice, that is, at 1 and 2 h after injection.

^{19}F MRI Acquisition Protocol. ^{19}F MRI experiments were performed in a Bruker 70/30 Bruker Biospec 7 T magnetic resonance scanner interfaced to an AVANCE III console and equipped with a BGA12 imaging gradient system. The acquisition of ^{19}F MRI images was done employing a customized RF quadrature surface design with two coils lying on a curve surface to fit the animal. A Butterfly arrangement and square loops were selected to shape the quadrature surface coil.[36,37] A nonmagnetic fixed- and variable capacitors were used to perform tuning and matching. In addition, a balun made of a semirigid cable and a capacitor was added to minimize unwanted common current modes.[38,39] The RF quadrature surface coil was mainly optimized to fluorine, but the coil can also be tuned for protons, which also allowed the acquisition of a reference proton image before the ^{19}F MRI recording. For details of each scanning condition, see the Supporting Information.

■ ASSOCIATED CONTENT

Supporting Information

The Supporting Information is available free of charge at https://pubs.acs.org/doi/10.1021/acsami.1c01291.

Full synthetic and characterization details for fluorinated building blocks and NPs; detailed protocols for *in vivo* experiments and tissue digestion for ICP-MS (PDF)

■ AUTHOR INFORMATION

Corresponding Author

Mónica Carril − *Instituto Biofisika UPV/EHU, CSIC, Leioa E-48940, Bizkaia, Spain; Departamento de Bioquímica y Biología Molecular, UPV/EHU, Leioa E-48940, Bizkaia, Spain; Ikerbasque, Basque Foundation for Science, Bilbao 48013, Spain;* orcid.org/0000-0002-1232-8658; Email: monica.carrilg@ehu.eus

Authors

Juan Manuel Arango − *Instituto Biofisika UPV/EHU, CSIC, Leioa E-48940, Bizkaia, Spain; Departamento de Bioquímica y Biología Molecular, UPV/EHU, Leioa E-48940, Bizkaia, Spain*

https://dx.doi.org/10.1021/acsami.1c01291
ACS Appl. Mater. Interfaces 2021, 13, 12941−12949

Daniel Padro − *Center for Cooperative Research in Biomaterials (CIC biomaGUNE), Basque Research and Technology Alliance (BRTA), Donostia-San Sebastián 20014, Spain*

Jorge Blanco − *Center for Cooperative Research in Biomaterials (CIC biomaGUNE), Basque Research and Technology Alliance (BRTA), Donostia-San Sebastián 20014, Spain*

Sonia Lopez-Fernandez − *Instituto Biofisika UPV/EHU, CSIC, Leioa E-48940, Bizkaia, Spain; Fundación Biofísica Bizkaia/Biofisika Bizkaia Fundazioa (FBB), Leioa E-48940, Spain*

Pilar Castellnou − *Center for Cooperative Research in Biomaterials (CIC biomaGUNE), Basque Research and Technology Alliance (BRTA), Donostia-San Sebastián 20014, Spain*

Palmira Villa-Valverde − *CAI Bioimagen Complutense, Unidad de RMN. Universidad Complutense, Madrid 28040, Spain; Departamento de Ingeniería Electrónica. Escuela Técnica Superior de Ingenieros de Telecomunicaciones, Universidad Politécnica de Madrid, Madrid 28040, Spain*

Jesús Ruiz-Cabello − *Center for Cooperative Research in Biomaterials (CIC biomaGUNE), Basque Research and Technology Alliance (BRTA), Donostia-San Sebastián 20014, Spain; CAI Bioimagen Complutense, Unidad de RMN. Universidad Complutense, Madrid 28040, Spain; Ikerbasque, Basque Foundation for Science, Bilbao 48013, Spain; Ciber de Enfermedades Respiratorias (Ciberes), Madrid 28029, Spain;* orcid.org/0000-0001-8681-5056

Abraham Martin − *Ikerbasque, Basque Foundation for Science, Bilbao 48013, Spain; Achucarro Basque Center for Neuroscience, Leioa E-48940, Spain*

Complete contact information is available at: https://pubs.acs.org/10.1021/acsami.1c01291

Notes

The authors declare no competing financial interest.

■ ACKNOWLEDGMENTS

This work was supported in part by grants from the Spanish State Research Agency (MCI/PID2019-107449RB-I00/AEI/10.13039/501100011033, RYC-2017-22412, and SAF2017-84494-C2-R), from the Fundación Biofísica Bizkaia, the Basque Excellence Research Centre (BERC) program, and projects IT1196-19 and Grant KK-2019/bmG19 of the Basque Government. We also thank the UE for funding (Nova MRI, H2020-MSCA-ITN-2018-811382). This work was performed under the Maria de Maeztu Units of Excellence Programme Grant MDM-2017-0720 ministry of Science, Innovation and Universities. The authors thank for technical and human support the Materials and Surfaces Service and the Central Analysis Service of Bizkaia provided by SGIker (UPV/EHU) and European funding (ERDF and ESF) for the XPS, TEM and ICP-AES analyses. The MRI service members of CIC biomaGUNE are also acknowledged for their support of the *in vivo* experiments.

■ REFERENCES

(1) O'Hagan, D. Understanding Organofluorine Chemistry. An Introduction to the C-F Bond. *Chem. Soc. Rev.* **2008**, *37*, 308−319.

(2) Liang, T.; Neumann, C. N.; Ritter, T. Introduction of Fluorine and Fluorine-Containing Functional Groups. *Angew. Chem., Int. Ed.* **2013**, *52*, 8214−8264.

(3) Wang, J.; Sánchez-Roselló, M.; Aceña, J. L.; del Pozo, C.; Sorochinsky, A. E.; Fustero, S.; Soloshonok, V. A.; Liu, H. Fluorine in Pharmaceutical Industry: Fluorine-Containing Drugs Introduced to the Market in the Last Decade (2001−2011). *Chem. Rev.* **2014**, *114*, 2432−2506.

(4) Purser, S.; Moore, P. R.; Swallow, S.; Gouverneur, V. Fluorine in Medicinal Chemistry. *Chem. Soc. Rev.* **2008**, *37*, 320−330.

(5) Cai, X.; Jin, R.; Wang, J.; Yue, D.; Jiang, Q.; Wu, Y.; Gu, Z. Bioreducible Fluorinated Peptide Dendrimers Capable of Circumventing Various Physiological Barriers for Highly Efficient and Safe Gene Delivery. *ACS Appl. Mater. Interfaces* **2016**, *8*, 5821−5832.

(6) Unione, L.; Alcalá, M.; Echeverria, B.; Serna, S.; Ardá, A.; Franconetti, A.; Cañada, F. J.; Diercks, T.; Reichardt, N.; Jiménez-Barbero, J. Fluoroacetamide Moieties as NMR Spectroscopy Probes for the Molecular Recognition of GlcNAc-Containing Sugars: Modulation of the CH-π Stacking Interactions by Different Fluorination Patterns. *Chem. - Eur. J.* **2017**, *23*, 3957−3965.

(7) Linclau, B.; Ardá, A.; Reichardt, N.-C.; Sollogoub, M.; Unione, L.; Vincent, S. P.; Jiménez-Barbero, J. Fluorinated Carbohydrates as Chemical Probes for Molecular Recognition Studies. Current Status and Perspectives. *Chem. Soc. Rev.* **2020**, *49*, 3863−3888.

(8) De Biasio, A.; Ibáñez de Opakua, A.; Bostock, M. J.; Nietlispach, D.; Diercks, T.; Blanco, F. J. A Generalized Approach for NMR Studies of Lipid-Protein Interactions Based on Sparse Fluorination of Acyl Chains. *Chem. Commun.* **2018**, *54*, 7306−7309.

(9) Tirotta, I.; Dichiarante, V.; Pigliacelli, C.; Cavallo, G.; Terraneo, G.; Bombelli, F. B.; Metrangolo, P.; Resnati, G. (19)F Magnetic Resonance Imaging (MRI): From Design of Materials to Clinical Applications. *Chem. Rev.* **2015**, *115*, 1106−1129.

(10) Gambino, G.; Gambino, T.; Pohmann, R.; Angelovski, G. A Ratiometric ^{19}F MR-Based Method for the Quantification of Ca^{2+} Using Responsive Paramagnetic Probes. *Chem. Commun.* **2020**, *56*, 3492−3495.

(11) Preslar, A. T.; Lilley, L. M.; Sato, K.; Zhang, S.; Chia, Z. K.; Stupp, S. I.; Meade, T. J. Calcium-Induced Morphological Transitions in Peptide Amphiphiles Detected by ^{19}F-Magnetic Resonance Imaging. *ACS Appl. Mater. Interfaces* **2017**, *9*, 39890−39894.

(12) Carril, M. Activatable Probes for Diagnosis and Biomarker Detection by MRI. *J. Mater. Chem. B* **2017**, *5*, 4332−4347.

(13) Celentano, W.; Neri, G.; Distante, F.; Li, M.; Messa, P.; Chirizzi, C.; Chaabane, L.; De Campo, F.; Metrangolo, P.; Baldelli Bombelli, F.; Cellesi, F. Design of Fluorinated Hyperbranched Polyether Copolymers for ^{19}F MRI Nanotheranostics. *Polym. Chem.* **2020**, *11*, 3951−3963.

(14) Zhang, C.; Moonshi, S. S.; Wang, W.; Ta, H. T.; Han, Y.; Han, F. Y.; Peng, H.; Král, P.; Rolfe, B. E.; Gooding, J. J.; Gaus, K.; Whittaker, A. K. High F-Content Perfluoropolyether-Based Nanoparticles for Targeted Detection of Breast Cancer by ^{19}F Magnetic Resonance and Optical Imaging. *ACS Nano* **2018**, *12*, 9162−9176.

(15) Hu, G.; Li, N.; Tang, J.; Xu, S.; Wang, L. A General and Facile Strategy to Fabricate Multifunctional Nanoprobes for Simultaneous ^{19}F Magnetic Resonance Imaging, Optical/Thermal Imaging, and Photothermal Therapy. *ACS Appl. Mater. Interfaces* **2016**, *8*, 22830−22838.

(16) Chen, H.; Song, M.; Tang, J.; Hu, G.; Xu, S.; Guo, Z.; Li, N.; Cui, J.; Zhang, X.; Chen, X.; Wang, L. Ultrahigh ^{19}F Loaded $Cu_{1.75}S$ Nanoprobes for Simultaneous ^{19}F Magnetic Resonance Imaging and Photothermal Therapy. *ACS Nano* **2016**, *10*, 1355−1362.

(17) Cui, J.; Jiang, R.; Guo, C.; Bai, X.; Xu, S.; Wang, L. Fluorine Grafted Cu_7S_4-Au Heterodimers for Multimodal Imaging Guided Photothermal Therapy with High Penetration Depth. *J. Am. Chem. Soc.* **2018**, *140*, 5890−5894.

(18) Boccalon, M.; Franchi, P.; Lucarini, M.; Delgado, J. J.; Sousa, F.; Stellacci, F.; Zucca, I.; Scotti, A.; Spreafico, R.; Pengo, P.; Pasquato, L. Gold Nanoparticles Protected by Fluorinated Ligands For ^{19}F MRI. *Chem. Commun.* **2013**, *49*, 8794−8796.

(19) Bidoggia, S.; Milocco, F.; Polizzi, S.; Canton, P.; Saccani, A.; Sanavio, B.; Krol, S.; Stellacci, F.; Pengo, P.; Pasquato, L. Fluorinated and Charged Hydrogenated Alkanethiolates Grafted on Gold:

Expanding the Diversity of Mixed-Monolayer Nanoparticles for Biological Applications. *Bioconjugate Chem.* **2017**, *28*, 43−52.
(20) Pengo, P.; Pasquato, L. Gold nanoparticles protected by fluorinated ligands: Syntheses, properties and applications. *J. Fluorine Chem.* **2015**, *177*, 2−10.
(21) Carril, M.; Padro, D.; Del Pino, P.; Carrillo-Carrion, C.; Gallego, M.; Parak, W. J. In Situ Detection of the Protein Corona in Complex Environments. *Nat. Commun.* **2017**, *8*, 1542.
(22) Padro, D.; Cienskowski, P.; Lopez-Fernandez, S.; Chakraborty, I.; Carrillo-Carrion, C.; Feliu, N.; Parak, W. J.; Carril, M. Toward Diffusion Measurements of Colloidal Nanoparticles in Biological Environments by Nuclear Magnetic Resonance. *Small* **2020**, *16*, No. e2001160.
(23) Michelena, O.; Padro, D.; Carrillo-Carrion, C.; del Pino, P.; Blanco, J.; Arnaiz, B.; Parak, W. J.; Carril, M. Novel Fluorinated Ligands for Gold Nanoparticle Labelling with Applications in ^{19}F-MRI. *Chem. Commun.* **2017**, *53*, 2447−2450.
(24) Ashur, I.; Allouche-Arnon, H.; Bar-Shir, A. Calcium Fluoride Nanocrystals: Tracers for In Vivo ^{19}F Magnetic Resonance Imaging. *Angew. Chem., Int. Ed.* **2018**, *57*, 7478−7482.
(25) Carrillo-Carrion, C.; Atabakhshi-Kashi, M.; Carril, M.; Khajeh, K.; Parak, W. J. Taking Advantage of Hydrophobic Fluorine Interactions for Self-Assembled Quantum Dots as a Delivery Platform for Enzymes. *Angew. Chem., Int. Ed.* **2018**, *57*, 5033−5036.
(26) Argudo, P. G.; Carril, M.; Martin-Romero, M. T.; Giner-Casares, J. J.; Carrillo-Carrion, C. Surface-Active Fluorinated Quantum Dots for Enhanced Cellular Uptake. *Chem. - Eur. J.* **2019**, *25*, 195−199.
(27) Argudo, P. G.; Martin-Romero, M. T.; Camacho, L.; Carril, M.; Carrillo-Carrion, C.; Giner-Casares, J. J. Fluorinated CdSe/Zns Quantum Dots: Interactions with Cell Membrane. *Colloids Surf., B* **2019**, *173*, 148−154.
(28) Carrillo-Carrion, C.; Gallego, M.; Parak, W. J.; Carril, M. Study of Fluorinated Quantum Dots-Protein Interactions at the Oil/Water Interface by Interfacial Surface Tension Changes. *Materials* **2018**, *11*, 750.
(29) Jacoby, C.; Temme, S.; Mayenfels, F.; Benoit, N.; Krafft, M. P.; Schubert, R.; Schrader, J.; Flögel, U. Probing Different Perfluorocarbons for in Vivo Inflammation Imaging by ^{19}F MRI: Image Reconstruction, Biological Half-Lives and Sensitivity. *NMR Biomed.* **2014**, *27*, 261−271.
(30) Cametti, M.; Crousse, B.; Metrangolo, P.; Milani, R.; Resnati, G. The fluorous effect in biomolecular applications. *Chem. Soc. Rev.* **2012**, *41*, 31−42.
(31) Zhang, C.; Liu, T.; Wang, W.; Bell, C. A.; Han, Y.; Fu, C.; Peng, H.; Tan, X.; Král, P.; Gaus, K.; Gooding, J. J.; Whittaker, A. K. Tuning of the Aggregation Behavior of Fluorinated Polymeric Nanoparticles for Improved Therapeutic Efficacy. *ACS Nano* **2020**, *14*, 7425−7434.
(32) Hens, Z.; Martins, J. C. A Solution NMR Toolbox for Characterizing the Surface Chemistry of Colloidal Nanocrystals. *Chem. Mater.* **2013**, *25*, 1211−1221.
(33) Werengowska-Ciećwierz, K.; Wiśniewski, M.; Terzyk, A. P.; Furmaniak, S. The Chemistry of Bioconjugation in Nanoparticles-Based Drug Delivery System. *Adv. Condens. Matter Phys.* **2015**, *2015*, 198175.
(34) Sperling, R. A.; Parak, W. J. Surface modification, functionalization and bioconjugation of colloidal inorganic nanoparticles. *Philos. Trans. R. Soc., A* **2010**, *368* (1915), 1333−1383.
(35) Huhn, J.; Carrillo-Carrion, C.; Soliman, M. G.; Pfeiffer, C.; Valdeperez, D.; Masood, A.; Chakraborty, I.; Zhu, L.; Gallego, M.; Yue, Z.; Carril, M.; Feliu, N.; Escudero, A.; Alkilany, A. M.; Pelaz, B.; del Pino, P.; Parak, W. J. Selected Standard Protocols for the Synthesis, Phase Transfer, and Characterization of Inorganic Colloidal Nanoparticles. *Chem. Mater.* **2017**, *29*, 399−461.
(36) Kumar, A.; Bottomley, P. A. Optimized quadrature surface coil designs. *MAGMA* **2008**, *21*, 41.
(37) Vaughan, J. T.; Griffiths, J. R. *RF Coils for MRI.*; Wiley, 2012.
(38) Villa-Valverde, P.; Rodríguez, I.; Padró, D.; Benito, M.; Garrido-Salmon, C. E.; Ruiz-Cabello, J. A dual ^{1}H/^{19}F birdcage coil for small animals at 7T MRI. *MAGMA* **2019**, *32*, 79−87.
(39) Peterson, D. M.; Beck, B. L.; Duensing, G. R.; Fitzsimmons, J. R. Common mode signal rejection methods for MRI: Reduction of cable shield currents for high static magnetic field systems. *Concepts Magn. Reson.* **2003**, *19B*, 1−8.

https://dx.doi.org/10.1021/acsami.1c01291
ACS Appl. Mater. Interfaces 2021, 13, 12941−12949